Title

In Situ Shape Control of Thermoplasmonic Gold Nanostars on Oxide Substrates for Hyperthermia-Mediated Cell Detachment

Journal

ACS Central Science, 6(11)

ISSN

2374-7943

Authors

Vinnacombe-Willson, Gail A
Chiang, Naihao
Scarabelli, Leonardo
et al.

Publication Date

2020-11-25

DOI

10.1021/acscentsci.0c01097

Peer reviewed

ACS central science

http://pubs.acs.org/journal/acscii

Research Article

In Situ Shape Control of Thermoplasmonic Gold Nanostars on Oxide Substrates for Hyperthermia-Mediated Cell Detachment

Gail A. Vinnacombe-Willson, Naihao Chiang, Leonardo Scarabelli,* Yuan Hu, Liv K. Heidenreich, Xi Li, Yao Gong, Derek T. Inouye, Timothy S. Fisher, Paul S. Weiss,* and Steven J. Jonas*

Cite This: *ACS Cent. Sci.* 2020, 6, 2105–2116

Read Online

ACCESS | Metrics & More | Article Recommendations | Supporting Information

ABSTRACT: Gold nanostars (AuNSTs) are biocompatible, have large surface areas, and are characterized by high near-infrared extinction, making them ideal for integration with technologies targeting biological applications. We have developed a robust and simple microfluidic method for the direct growth of anisotropic AuNSTs on oxide substrates including indium tin oxide and glass. The synthesis was optimized to yield AuNSTs with high anisotropy, branching, uniformity, and density in batch and microfluidic systems for optimal light-to-heat conversion upon laser irradiation. Surface-enhanced Raman scattering spectra and mesoscale temperature measurements were combined with spatially correlated scanning electron microscopy to monitor nanostar and ligand stability and microbubble formation at different laser fluences. The capability of the platform for generating controlled localized heating was used to explore hyperthermia-assisted detachment of adherent glioblastoma cells (U87-GFP) grafted to the capillary walls. Both flow and laser fluence can be tuned to induce different biological responses, such as ablation, cell deformation, release of intracellular components, and the removal of intact cells. Ultimately, this platform has potential applications in biological and chemical sensing, hyperthermia-mediated drug delivery, and microfluidic soft-release of grafted cells with single-cell specificity.

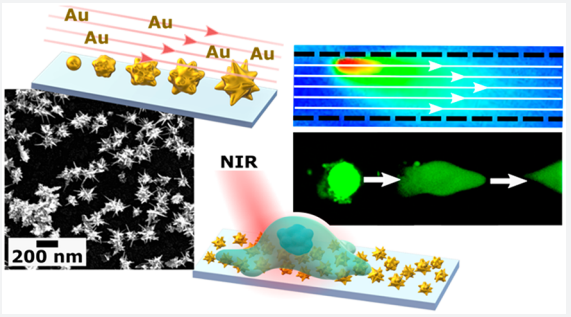

Gold nanoparticles (AuNPs) with dimensions smaller than the wavelength of light can produce intense nanoscale electromagnetic field enhancement. Together with their biocompatibility and chemical stability, the plasmonic properties of AuNPs offer unique opportunities for a variety of biomedical applications.[1−3] When the AuNPs are illuminated, there are collective excitations of the conduction electrons known as localized surface plasmon resonances (LSPRs). The plasmon resonance oscillation frequencies can be tuned by altering particle size, shape, and local dielectric environment.[4] Developments in bottom-up wet-chemical synthetic methodologies, in particular the seed-mediated growth method, have improved the accessibility of uniform colloidal suspensions of nanoparticles with well-controlled shapes.[4−9] In the seed-mediated method, gold nuclei or "seeds" are formed from gold salt reduction and are subsequently added to a growth solution containing additional gold precursor and shape directing reagents to produce colloidal suspensions of shapes with LSPRs in the near-infrared (NIR) biological window such as gold rods, shells, cages, and stars.[10] Nonradiative plasmon-phonon coupling enables rapid local thermalization in these structures,[11] and this property has been leveraged for numerous studies focused on tissue-nanoparticle interactions.[12−15] Among these NIR-responsive morphologies, gold nanostars (AuNSTs) have gained particular interest due to the significant electromagnetic field enhancement at their sharp points,[16,17] high NIR extinction, and large surface areas.[18,19]

Many researchers have integrated plasmonic nanostructures into solid-state systems such as sensors,[20−22] cargo delivery platforms,[23,24] substrates for light-responsive cell retrieval,[25,26] materials for combined cancer cell hyperthermia/chemotherapies,[12,27,28] and fundamental studies on phenomena resulting from plasmonic heating (*e.g.*, bubble generation).[29−31] There exist several strategies for nanoparticle integration into such systems, where direct functionalization with presynthesized nanoparticles (*i.e.*, applying self-assembly, lithography, or a combination of the two)[32−36] and direct nanoparticle synthesis[37−43] on the desired substrate offer common approaches toward achieving surface decoration with crystalline products. Despite these significant developments, nanoparticle integration approaches still face challenges accessing different substrate geometries, such as tubing and curved features, which are of broad interest for developing

Received: August 15, 2020
Published: October 23, 2020

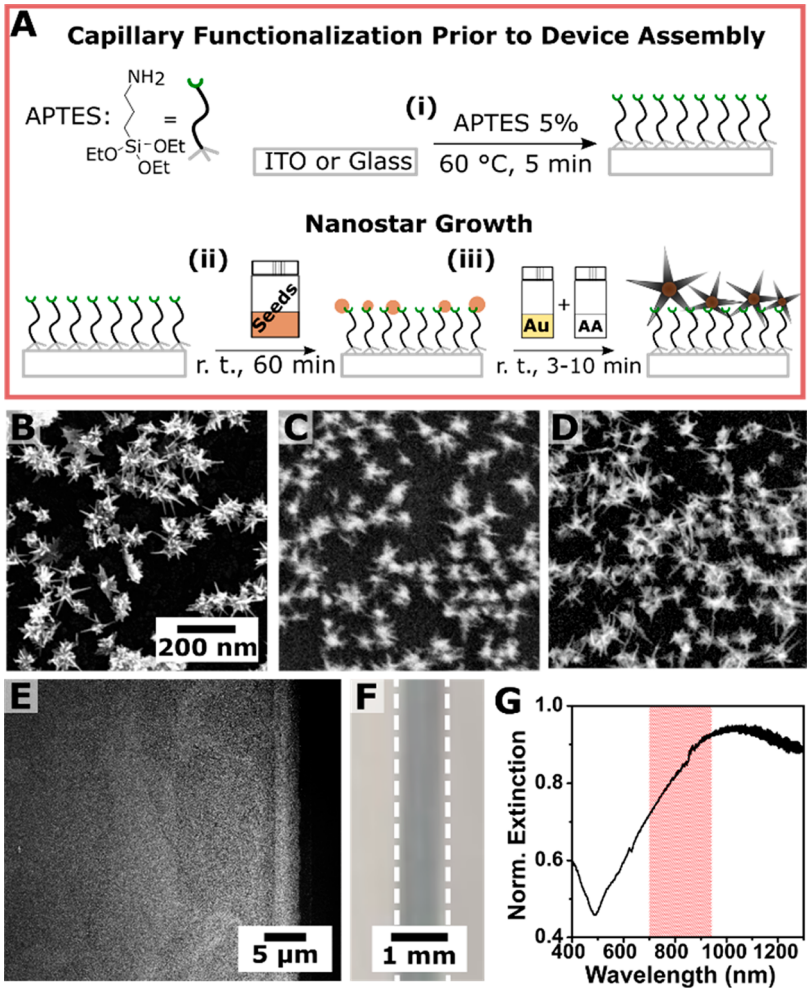

Figure 1. (A) Schematic of *in situ* seed-mediated gold nanostar growth: (i) indium tin oxide (ITO) and glass surface functionalization with aminopropyltriethoxysilane (APTES), (ii) attachment of catalytic seeds, and (iii) incubation (10 min) or flow (3 min) of growth solution containing tetrachloroauric acid, silver nitrate, laurylsulfobetaine, and ascorbic acid (AA). Scanning electron micrographs of gold nanostars on (B) ITO and (C) glass slides, and (D, E) within glass microcapillaries (all shown at the same scale). (F) Photograph showing blue capillary coloration following flow of growth solution and (G) ultraviolet−visible spectrum of the nanostar-coated capillary. The red area indicates the first near-infrared biological window.

substrates that uniquely interact with light, microfluidic platforms, and plasmonic scaffolds for biological studies.[44] The development of a robust method for generating substrates functionalized with size- and shape-controlled nanoparticles at high density remains elusive and an active research challenge.[45]

Here, we report a facile method for the generation of AuNSTs on oxide substrates by applying a versatile silane functionalization method and bottom-up wet-chemical synthesis. Protocols for the synthesis of AuNST colloidal suspensions were adapted by first grafting colloidally synthesized seeds and performing subsequent shape control *in situ* by simply submerging the functionalized surface in a growth solution. Within a microfluidic capillary, the flow rate and time of the growth solution were used to control the morphology and aspect ratio of the AuNSTs. Systematically varying flow parameters, we achieved highly branched nanostructures with configurable aspect ratios in the microfluidic capillary. These structures exhibit efficient light-to-heat conversion when irradiated with NIR light. The mesoscale heating of the microcapillary can be controlled by adjusting the laser power, as well as by flowing water into AuNST-decorated microcapillaries at different rates. Changes in the overall mesoscale temperature were correlated with phenomena at the local nanoscale environment through simultaneous thermal and surface-enhanced Raman scattering (SERS) measurements. Moreover, these nanostructures are interesting and useful for a variety of biomedical applications, such as photothermal therapy, due to their plasmonic response to NIR light and biocompatibility; thus, we applied this system to interrogate the response of adhered glioblastoma cells to AuNST localized heating and identified conditions that facilitate the systematic detachment of single cells from the capillary walls. Cellular responses, such as reshaping, necrosis/membrane permeabilization, and rapid cell ablation were dependent on local heating and flow conditions. Our results suggest that this plasmonic-nanostructure-integrated microfluidic platform will offer new solutions for small-molecule sensing,[20] intracellular delivery via poration,[24,46] or the targeted retrieval of single cells in adherent cultures, representing a starting point for the development of devices capable of cell capture and targeted, selective light-triggered release.[25,26]

https://dx.doi.org/10.1021/acscentsci.0c01097
ACS Cent. Sci. 2020, 6, 2105−2116

RESULTS AND DISCUSSION

***In Situ* Surface Growth of Gold Nanostars.** Gold nanostars with high aspect ratios and numbers of branches efficiently produce intense localized heat in response to NIR light.[47,48] Of the various bottom-up wet-chemical approaches for synthesizing branched nanoparticles, the seed-mediated growth method, where nucleation and growth steps are performed separately and sequentially, is one of the most promising approaches for precise nanoparticle shape control.[4−9] However, the immobilization of presynthesized nanoparticles on substrates can result in low surface density and inhomogeneous distributions.[41,45] To address this limitation, we developed a seed-mediated synthetic method, enabling direct growth of shape-controlled AuNPs uniformly on oxide substrates, based on recent methods utilized to achieve branched structures on surfaces using *in situ* shape control.[25,49] In particular, we modified a previously established batch seed-mediated growth protocol from Pallavicini and coworkers,[50] improving product reproducibility and reducing the impact of secondary nucleation (*i.e.*, uncontrolled formation of new nuclei after particle growth has already begun). In the original approach, zwitterionic surfactant laurylsulfobetaine (LSB) yields rapid growth of nanostars, utilizing kinetic control to achieve sharp tips. In their synthesis, the seeds were also capped with LSB, resulting in the requirement that reagents were kept at low temperature to avoid rapid aging and batch-to-batch variation in the position and intensity of the LSPR peaks. Therefore, we instead opted to utilize cetyltrimethylammonium chloride (CTAC)-capped seeds, which age more slowly and yield products with reproducible spectra (Figure S1). Moreover, the addition of ascorbic acid (reducing agent) in the absence of the seeds results in fast secondary nucleation, leading to the uncontrolled growth of suboptimal morphologies. Thus, we further modified the growth solution through addition of hydrochloric acid (HCl) to slow secondary nanoparticle nucleation in solution. Ultraviolet− (UV−) visible kinetic data provided in Figure S2 indicate that significant nucleation does not occur for at least 20−40 min following ascorbic acid addition, unless the gold seeds are added to the growth medium. The final adjusted colloidal protocol produced three major products, as observed by transmission electron microscopy (TEM) and UV−vis spectroscopy: anisotropic spheroids, low-aspect ratio AuNSTs, and high-aspect ratio AuNSTs (Figure S3A−D), exhibiting LSPR peaks at *ca.* 525, 650, and 875 nm, respectively. The corresponding yield of high-aspect ratio products was 20% (Figure S3E−G). Addition of HCl slows the growth process and disfavors formation of highly branched and high aspect ratio products.[7] However, even without HCl addition, three different products are observed, indicating that the low yield of the desired products is likely due to inevitable secondary nucleation in solution. As discussed below, secondary nucleation is reduced by growing the branched structures directly on planar substrates.

The *in situ* seed-mediated AuNST growth strategy developed here takes advantage of the size of presynthesized seeds, which can be grafted easily onto a variety of oxide materials, followed by shape control *in situ*. The *in situ* growth method approach is summarized in detail in Figure 1A: (i) substrate chemical modification with (3-aminopropyl)-triethoxysilane (APTES), (ii) grafting presynthesized gold seeds onto the APTES chemical anchor to serve as catalytic surfaces for the growth of AuNSTs, and (iii) subsequent introduction of a growth solution via incubation or flow. Attaching the smaller seed particles prior to AuNST growth, rather than tethering larger presynthesized nanostructures to the substrates, improves product density and limits the formation of byproducts resulting from secondary nucleation events that normally occur during the colloidal growth step. Moreover, our methodology can be applied to a variety of substrate geometries, including glass microcapillaries, enabling straightforward integration with microfluidic devices, which are increasingly applied for the development of biomedical devices and platforms.[51−54]

Compared to previous work, the functionalization of our substrates with the plasmonic structures is rapid and applies only bottom-up wet-chemical techniques, avoiding the need for templating, printing, or thermal/electrochemical deposition. This strategy enables us to integrate the plasmonic structures with more complex substrate geometries, such as glass tubing and microfluidic capillaries, which are of great interest for the development of sensors and devices probing biological systems.[44] By translating optimized parameters for colloidal synthesis to substrate-mediated growth, we achieved uniform AuNST coatings on indium tin oxide (ITO) (Figure 1B), glass slides (Figure 1C), and along the internal walls of glass microcapillaries (Figure 1D,E). The final products yield films that appear blue in color with a broad LSPR peak at *ca.* 975 nm after flowing growth solution for 3 min (Figure 1F,G). Silver nitrate is known to play important roles in the shape control of anisotropic nanoparticles.[6] Reoptimization of the silver concentration in the growth solution confirmed that nanostructures giving the highest NIR extinction were produced with the same concentration used for the colloidal suspension (Figure S4). This observation suggests that the optimal colloidal shape-directing reagent concentrations are directly translatable to growth in flow. The AuNSTs grown *in situ* were characterized by scanning electron microscopy (SEM) and were found to have branches with average aspect ratio of 3 ± 1, and an average of 7 ± 2 branches per AuNST without accounting for hyperbranching (n = 3, 150 nanoparticles each). Moreover, flow can increase the rate at which the gold precursor is delivered to the surface-bound seeds, therefore requiring shorter growth times (3 min) to achieve branched products in flow compared to the 10 min growth time necessary for slides or wafers. The AuNSTs grown *in situ* on flat substrates and in rectangular microcapillaries had 2.4× higher average aspect ratio and nearly twice the branching of those synthesized in solution (histograms of the *in situ*-grown AuNSTs are provided in Figure S5, Table S1). On the substrate, the effective ratio of gold precursor to the seeds depends on factors absent in standard colloidal growth, including the yield of APTES functionalization and seed deposition. In the case of the microfluidic capillary, the flow profile, and rate must also be considered. Given these factors, the higher yield of high aspect ratio products on both the flat substrates and the capillary can be attributed to the spatial restrictions for growth from the surface-bound seeds. Furthermore, byproduct deposition is prevented by removal of the substrates from the growth solution or by flowing the growth solution out of the capillary prior to significant secondary nucleation.

When the synthesis is performed under flow, there are several factors affecting nanoparticle morphology, such as the volume of growth solution passed through the microfluidic

https://dx.doi.org/10.1021/acscentsci.0c01097
ACS Cent. Sci. 2020, 6, 2105−2116

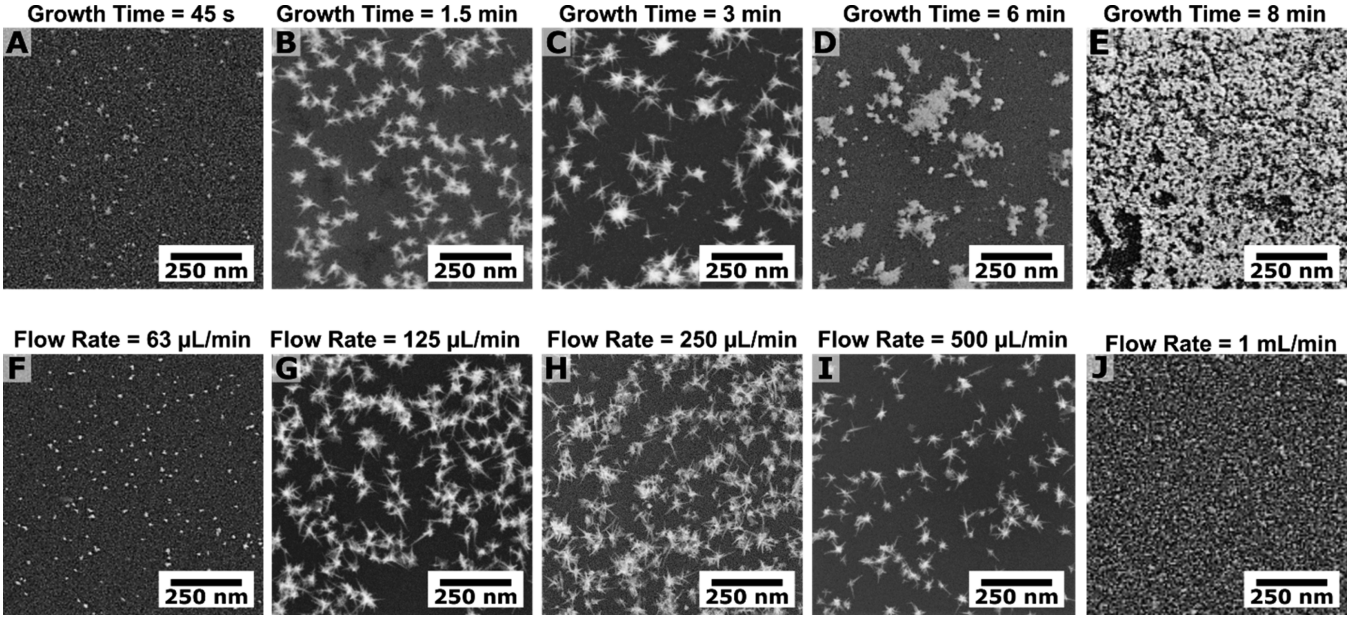

Figure 2. (A–E) Gold nanostars grown at the various growth times shown, all with flow rate 125 μL/min and (F–J) flow rates, all with 3 min growth times. Products shown in panels C and H represent the standard growth conditions.

channel, *i.e.*, the "growth time" (Figure 2A–E), and the flow rate used (Figure 2F–J). Nanostars grown over short time periods lacked branching, likely due to insufficient quantities of growth solution within the microcapillary (Figure 2A). Nanostructures grown for greater than 8 min at the same flow rate produced overgrown nanoparticle films, consistent with the introduction of excess gold precursor (Figure 2E). Conditions generating products shown in Figure 2C,H have 3 min 3 mingrowth times, which ensured that enough growth solution passed through the microfluidic system without leading to significant secondary nucleation (Figure S2) and appear to yield the desired highly branched, high aspect ratio products more reproducibly than those grown at different flow rates (Figure S6). Assuming lateral diffusion was negligible, the flow rate should dictate the deposition of gold atoms onto the seeds, where faster flow rates are expected to produce structures with the highest anisotropy and branching. However, both the lowest and highest flow rates yielded particles with minimal branching and low aspect ratio (Figure 2F,J). We expect that several factors affect the spatial distributions of the nanostructures, including variabilities in the flow rate and profile within the capillaries due to sample-to-sample differences in capillary positioning within the tubing, the yield of APTES functionalization, and seed anchoring. Specifically, the positioning of the capillary has the potential to affect the flow profile of the growth solution and the APTES layer is known to be inhomogeneous.[55] However, considering these effects, we achieve sufficient density of the nanostructures on the substrate (Figure 1). The branched particles were synthesized under laminar conditions (Reynolds' number, $R_e \sim 8.5$), and we infer that the flow has a profound effect on AuNST morphology, since the products found at the outlet of the capillary have much less branching than those present at the inlet and center (Figure S7). This observation suggests that an alternative flow profile (*i.e.*, that facilitates interaction of reagents with the internal capillary walls through mixing, or introducing lateral flows, such as Dean flow)[56] would likely offer improved control over product selection. This strategy will be tested in future studies. Ultimately, the optimized *in situ* synthetic parameters provide a useful method for functionalizing oxide substrates of arbitrary geometries with dense coatings of shape-controlled products and demonstrate the potential for accessing different nanoparticle morphologies offered by the careful design and incorporation of fluid flow into the synthesis.

Plasmonic Activity and Photothermal Response Characterization. Cell hyperthermia can be broken down into temperature regimes giving rise to different biological phenomena: 37–41 °C is the diathermia range, where cells are able to maintain homeostasis and do not undergo significant damage due to heating; for 41–48 °C, cell death can be achieved and protein unfolding and aggregation occurs; 48–60 °C constitutes the ablation regime where thermalization yields DNA damage and rapid, irreversible protein denaturation.[57] Plasmonic heating is a near-field effect that can be detected by far-field temperature changes as heat is transferred from the nanoparticle to the surroundings.[58] We characterized the photothermal performance of the prepared substrates by measuring the mesoscale temperature using a thermal camera as the AuNST-coated microcapillary was irradiated at different laser power densities with a 785 nm continuous wave (cw) laser and under different flow conditions. The thermal camera measures the temperature of the outer capillary surface, because the infrared radiation inside the capillary does not transmit through the capillary wall. However, because the capillary wall is thin, the temperature gradient through the wall can be neglected, and the capillary surface temperatures are used to approximate the fluid temperatures inside the capillary. Temperature changes (ΔT) of *ca.* 40 °C were observed in "no flow" (stationary liquid) conditions (Figure 3A). When cooling (via flowing liquid) was applied at the same power density, temperature changes of 10 °C were observed (Figure 3B). Without flow, equilibrium temperature was reached after ~10 s of irradiation, compared to less than 1 s with flow. Rapid cooling occurred once laser irradiation was discontinued (Figure 3C,D). Negligible changes in temperature were

https://dx.doi.org/10.1021/acscentsci.0c01097
ACS Cent. Sci. 2020, 6, 2105–2116

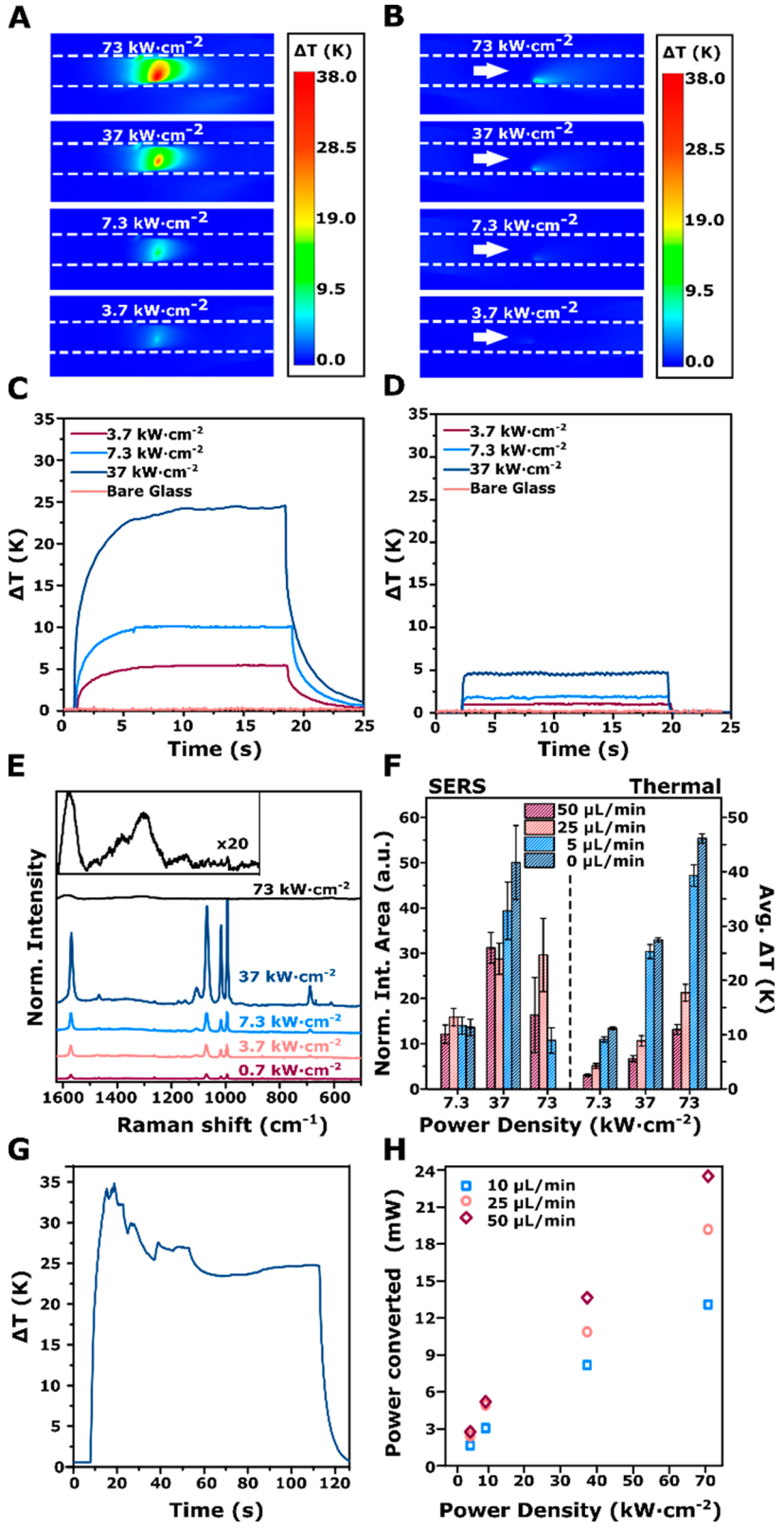

Figure 3. Thermal camera images of gold-nanostar-coated capillaries irradiated at different laser power in part A, no flow, and part B, 50 μL/min flow. The dotted line indicates the edges of the capillary (width: 1 mm) Heating curves in part C, no flow, and part D, 50 μL/min flow. (E) Surface-enhanced Raman spectra of thiophenol at various laser power (no flow), and the Raman spectra showing amorphous carbon obtained at 73 kW·cm^{-2} at 20× intensity (inset). (F) Comparison of Raman normalized integrated peak area at 1581 cm^{-1} and measured mesoscale heating at different flow conditions and laser power. (G) Heating profile of capillary at high power density. (H) Average power converted to heat at different laser power densities (maximum laser power is 25 mW). Waterfall plots of Raman spectra over a 5 min-period are shown in Figure S9 in the Supporting Information. Additional data on the thermal performance and scanning electron micrographs of products before and after reshaping are shown in Figures S10–S12. Laser wavelength: 785 nm.

https://dx.doi.org/10.1021/acscentsci.0c01097
ACS Cent. Sci. 2020, 6, 2105−2116

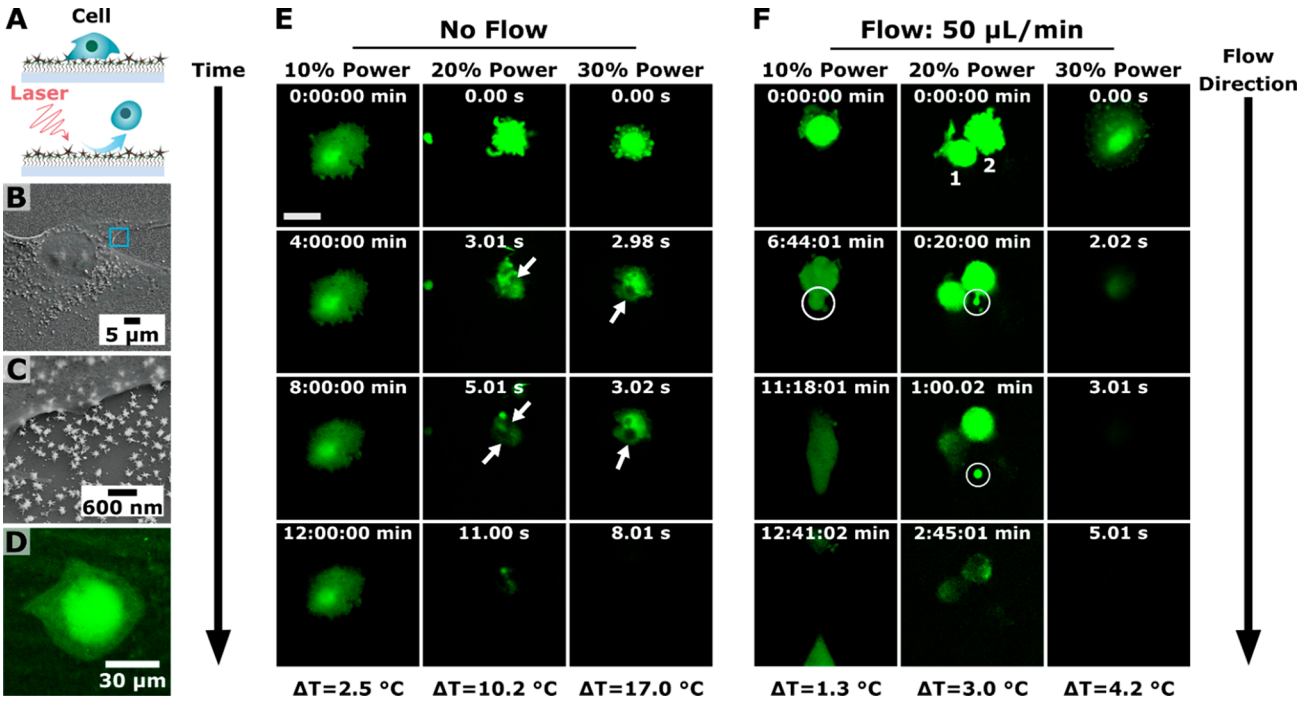

Figure 4. (A) Schematic of adherent cell attachment and light-activated removal. (B, C) Scanning electron micrographs (additional images shown in Figure S11) and (D) scanning fluorescence confocal microscopy image of a green fluorescent protein (GFP)-expressing U-87 cell on gold nanostars. Scanning fluorescence confocal microscopy images of cell response at different laser fluences in part E, no flow (white arrows indicate microbubbles), and in part F, 50 μL/min flow rate (white circles indicate blebs which caused leaking of intracellular contents—see Supplementary Videos S1−S10) (scale bar = 25 μm; parts E and F shown at the same scale. Maximum fluence = 17 mJ/cm^2, Tables S2 and S3). Laser wavelength: 785 nm.

measured when an unfunctionalized capillary was irradiated, consistent with the heating being due to the plasmonic response of the AuNSTs (Figure S8).

Because nanophotothermolysis is a near-field phenomenon, the measured macroscale or mesoscale temperatures are much lower than the temperature at the nanoparticle surface, which can exceed hundreds of degrees Celsius.[29] Rapid local thermalization can result in a number of events, including damage to molecules bound to the nanostructures, nanoparticle reshaping, and vaporization/cavitation of fluid immediately surrounding the nanoparticles to produce nano- and microbubbles.[11,29−31,59,60] The plasmonic activity of the nanoparticles should not be affected by the presence of flowing water. Consequently, although the reported mesoscale temperatures in flow are lower than those seen under static conditions, we hypothesized that the nanoscale temperatures are comparable regardless of the flow. To test this hypothesis, we probed the near-field environment by measuring the SERS signal for AuNST-bound thiolated ligands. In fact, both the high SERS enhancement and the heat generation in branched AuNPs results from high electric field localization at sharp points.[17,61,62] Additionally, phenomena such as tip rounding and reshaping of the nanostructures, as well as damage to the ligand coating can occur at high temperatures, reducing both light-to-heat conversion and SERS intensity. Therefore, the combination of near-field and far-field optical measurements can lead to better assessment and understanding of the nanoscale effects of flow over the photothermal process. Such measurements are challenging to obtain simultaneously and in real-time; however, we have developed and set up experiments enabling us to do so (Figures S16 and S17).

Experimentally, the LSB coating on the AuNSTs was displaced by thiophenol, a common nonresonant model system for SERS studies, taking advantage of the strong gold−thiol interaction. To track both the mesoscale temperature of the capillary (*i.e*, probing the far field) and the SERS signal of the thiols bound to the nanostructures (*i.e.*, probing the near field), we incorporated concurrent thermal camera measurements along with the collection of SERS spectra in aqueous solution as well as in phosphate-buffered saline (PBS) and in cell culture medium, since these systems may be of interest for biological applications (Figure S9). As expected, both temperature and SERS intensity increase with laser power (Figure 3A−E). Although the mesoscale temperature decreases significantly under flow, the SERS intensity remains comparable at flow rates ranging between 0 and 50 μL/min and at laser fluences up to the highest power density tested (73 kW·cm^{-2}; Figure 3F). However, under stationary conditions we observed the disappearance of the thiophenol fingerprints at the highest power density tested (73 kW·cm^{-2}) together with the appearance of the Raman spectra for amorphous carbon (*ca.* 1400 cm^{-1}, Figure 3E). The decrease in signal could be due to damage (*i.e.*, breaking bonds within the molecule) or desorption of the molecule from the nanostars. Although desorption cannot be ruled out, the appearance of amorphous carbon peaks indicates that damage to the ligand does occur. Furthermore, at the same power density (73 kW·cm^{-2}, Figure 3G), we observed a decrease in ΔT over time, indicating that there was reduced light-to-heat conversion, pointing toward nanoparticle reshaping. Spatially correlated SEM measurements provide further evidence that nanoparticle restructuring occurs under these conditions (Figure S10C). We conclude that the cooling effects of the fluid flow protect the

https://dx.doi.org/10.1021/acscentsci.0c01097
ACS Cent. Sci. 2020, 6, 2105−2116

nanostructures from thermally induced reshaping. Furthermore, we observed the formation of bubbles large enough (*i.e.*, several microns in diameter based on the microscope images) to result in measurable mesoscale temperature fluctuations of a few degrees as they refill and coalesce with one another (Figure 3G shows the temperature fluctuations during this process).

The comparable SERS intensities observed under the various flow conditions indicate that although the presence of flowing liquid alters the mesoscale temperature, and flowing water can thereby reduce ligand damage or AuNST reshaping, it ultimately does not affect the near-field generation of heat. To test if the light-to-heat conversion is independent of the flow conditions (*i.e.*, when damage to the plasmonic structures does not occur), we estimated the heat q for different flow rates at multiple laser power settings (see Supporting Information, Figures S11 and S12 and corresponding discussion). Based on the power of the laser source X (W), the power absorbed as heat is approximately q/X%. For different flow rates, the laser power converted into heat increases linearly with the percentage of the laser power and is comparable for the three different flow rates (Figure 3H). We estimate up to ∼90% power conversion (based on the ∼24 mW power converted compared to the max laser power of 25 mW) into heat from our estimation of the steady state ΔT at 50 μL/min flow rate, which lies within the expected performance previously reported for branched structures in colloidal suspension.[63,64] These results provide additional support that the flow conditions do not alter the plasmonic activity of the nanostructures within the capillary.

In summary, we demonstrate that these simultaneous SERS-thermal measurements can be correlated to far-field and near-field plasmonic responses of the AuNSTs and can be applied as tools for probing the nanoscale environment. In addition, we find that tuning the microfluidic flow rate enables finer control over total capillary heating without sacrificing plasmonic activity and has potential for protecting the nanostructures from temperature-induced morphological changes.

Nanophotothermolysis of Adherent Cells. Microfluidic systems have previously been proposed to confine adherent and suspension cells spatially to the same focal plane for performing fluorescence confocal microscopy studies on apoptosis and cell response to chemotherapeutics.[53,54,65] Fluorescence confocal cell imaging and simultaneous monitoring of the mesoscale temperature change has potential to offer new insight into the temperature dependence of cellular responses to plasmonic heating as they occur in real-time. Our setup enables us to use laser-scanning fluorescence confocal microscopy to visualize AuNST-cell interactions with adherent cells while irradiating the AuNSTs with a NIR fs-pulsed laser and measuring capillary temperature (Figure S17). Moreover, we demonstrated hyperthermia-mediated single-cell "point-and-shoot" release of grafted adherent cells (Figure 4A) and observe changes in cell morphology, appearance of necrotic blebs, and microbubble formation, depending on the flow rate and temperature.

First, we evaluated the adhesion of model cells onto AuNSTs by culturing them over a AuNST-coated substrate. Here, our goal is to functionalize the nanostructures with extracellular matrix proteins that promote cell growth and adherence. Thiols bind strongly to gold, and thus we used mercaptoundecanol (MUD) to ensure displacement of LSB. Modification with MUD provides a hydroxyl functionality to facilitate coating with fibronectin in order to enhance cell interactions with the AuNSTs (*NB*: total thickness of the AuNST coating is ∼25 nm).[66,67] After functionalization, the AuNST-capillary was split and an adherent glioblastoma cell line expressing green fluorescence protein (U-87 GFP) was incubated on the substrate in a well plate for 24 h (at 37 °C, 95% humidity, 5% CO_2). Scanning electron micrographs and fluorescence confocal microscopy images show that the cells spread over the functionalized substrate (Figure 4B−D). When cells were administered into the capillary via flow, spreading was observed within 60 min (Figure S12). This analysis shows that the functionalization procedure enables direct interactions of the cell membrane with the local environment of the plasmonic nanostructures.

Plasmonic heating has previously been utilized to detach cells from planar substrates at time scales of up to ∼1 h.[25,26] Our work builds upon these previous developments by applying the *in situ* growth method we developed to achieve point-and-shoot release of grafted cells with *single-cell* specificity. The point-and-shoot release triggered by the localized heating demonstrates the plasmonic activity and the continued potential of our system for additional biological applications (Figure 4A). The cells were flowed into the capillary and incubated within the capillary for 60 min to facilitate attachment (based on the initial SEM/fluorescence confocal microscopy data, Figure S14), then irradiated in the capillary. Though thermal measurements and microscopy imaging are generally performed separately,[68,69] here we apply the setup shown in Figure S17 to perform *simultaneous* thermal imaging and laser scanning confocal measurements while irradiating the capillary with a 785 nm femtosecond-pulse laser (80 MHz rep rate, 35 fs pulse width). This experimental setup enabled us to observe cell morphology changes, blebbing, loss of cytoplasmic material, bubble formation, and removal from the substrate of single cells in real time within a ΔT range from ∼1 to 30 °C. It was observed that without fluid flow, cell removal occurs quickly with increased maximum temperature, where rapid cell ablation is observed within seconds as ΔT approaches 20 °C. Furthermore, if the irradiation area in the capillary temperature is increased by more than *ca.* 10 °C, we observed the formation of microbubbles (Figure 4E). Steam nanobubble generation and subsequent formation of microbubbles via diffusion of dissolved gases has been previously described for substrates (such as glass slides) decorated with thermoplasmonic nanoparticles, and their formation has been shown to play a role in causing mechanical damage to cell membranes.[13] Air bubble formation requires local temperatures near the spinodal temperature of water (277 °C) and consequently the local heat energy produced in this system is likely to exceed the measured mesoscale capillary heating greatly.[29,60] Bubble formation during nanophotothermolysis of cells induces significant mechanical stress, which likely plays major roles in the mechanism of cell removal under these circumstances.[59,70] As a control experiment, we observe no cell damage, bubble formation, nor significant temperature change for at least 5 min irradiation time up to 30% of the fs-pulsed laser power (17 mJ/cm^2; Tables S2 and S3) when AuNSTs are not present in the capillary (Figure S13).

Under flow (Figure 4F), significant cell membrane damage occurs with temperature changes above 4 °C, and ablation leads to the loss of intracellular materials and near instantaneous removal from the substrate (*i.e.*, similar to what was observed at 17 °C without flow). At the fluences

https://dx.doi.org/10.1021/acscentsci.0c01097
ACS Cent. Sci. 2020, 6, 2105−2116

tested (5.7−17 mJ/cm^2), we do not observe microbubbles, which may be due to the flowing liquid carrying the bubbles downstream. However, even in the absence of microbubbles, cells exhibit membrane damage with changes in temperature of only 1−3 °C, leading to the rapid formation of protrusions called "blebs," with diameters in the tens of microns, which are precursors to the release of intracellular contents. The formation of blebs indicates rupture of the outer cell membrane and the nature of the blebbing can also indicate different mechanisms of cell death, such as apoptosis or necrosis, which have been observed previously with nanoparticle hyperthermia.[12,71−73] Apoptosis is a biologically controlled process, whereas necrosis is rapid cell death caused by external stimuli (*e.g.*, high local temperature in this case). The size and degree of blebbing indicates necrosis as the primary mechanism of cell removal and damage. Note that without flow, the formation of blebs is harder to detect using confocal microscopy, as the blebs quickly move out of the focal plane and do not move around nor detach from the main body of cells exposed to fluid flow.

The rate of local temperature increase is important to control when studying cell interactions with thermoplasmonic nanoparticles, where selection between apoptosis and necrosis can be achieved through careful control of the heating conditions. Furthermore, we leverage gradual heating to demonstrate controlled release of cultured cells from substrates with branched thermoplasmonic structures.[25] In our system, we are able to tune both the flow and the laser fluence systematically to control the heating experienced by the cells. Although the laser fluences (11 mJ/cm^2) giving ΔT of 10 and 3 °C without and with flow, respectively, are the same, the cooling effects of flow mitigate damage to the cell, enabling cells to remain on the substrate substantially longer. With flow, we also do not observe bubble formation, likely because any bubbles generated are rapidly carried downstream. Both with and without flow, the cells exhibit significant membrane disruption, even at low overall capillary temperatures. In these experiments, we utilize a femtosecond-pulse laser to trigger the plasmonic response, which might result in more aggressive localized heating compared to cw illumination sources, where the energy deposition and generation of heat can be more efficiently controlled.[11,74,75] The SERS experiments (cw laser) and the cell experiments (femtosecond pulsed laser) exhibit similar photothermal phenomena (*i.e.*, bubble formation, AuNST reshaping), but we note that these systems are not directly comparable in their deposition of energy to the particles and therefore the mechanisms leading to the resulting phenomena likely differ between the two illumination conditions. Thus, building upon what was done here, one interesting avenue to pursue will be to compare temperature measurements, SERS spectra, and fluorescence confocal cell images collected simultaneously in real time with different illumination sources to probe phenomena that result from intense nanoscale heat generation.

CONCLUSIONS AND PROSPECTS

We developed a seeded-growth method to achieve AuNST growth *in situ* on substrates with arbitrary geometries and that found this approach leads to improved selection of highly anisotropic products. On the basis of this protocol, we developed a wet-chemical approach for growing shape-controlled nanoparticles not only on planar substrates but also on substrates with arbitrary geometries, such as glass microcapillaries using microfluidics. For the microfluidic growth, we demonstrate that both growth time and flow rate can be tuned to manipulate AuNST morphology. Our optimization of the branched structures in flow indicates that the rational design of flow profiles, rates, and growth times can be used to access different nanoparticle morphologies, offering the prospect of exploring new growth mechanisms for different shaped nanoparticles in microfluidics. Upon illumination, the AuNST coatings exhibit intense local heating, achieving up to ∼40 °C mesoscale temperature increase, and flowing water acts as a heat sink, mitigating overall capillary heating. We developed an experimental setup for simultaneous measurement of thermal fluctuations and SERS signal, and apply this system to monitor damage to ligands and heat-induced changes to AuNST morphology occurring at the nanoscale in real time. We have demonstrated light-triggered "point-and-shoot" selective removal of cells from the substrate and were able to observe cell necrosis, ablation, microbubble formation, and intact cell removal depending on flow conditions and laser fluence. With and without visibly evident microbubble formation, AuNST photothermal response leads to cell membrane damage, causing their rapid removal from the substrate. Due to the robustness of gold−thiol interactions, the use of thiolated antibodies to facilitate capture and selection of specific cell types adds additional experimental versatility and device capabilities while opening areas for future studies that apply our approach to biomedical applications. Although the presented studies on adherent cell interactions with AuNSTs in flow are preliminary, these data indicate that future studies elucidating the interplay between temperature, flow, and cell-AuNST interaction strength can be leveraged to identify conditions that support controlled removal of intact, viable cells. Later designs of the platform will target soft-release of disease-relevant cells, incorporating systems for selective release and collection of specific cells from a large background cell population via localized heating to enable analysis of cell viability via colorimetric or flow cytometry-based assays and opportunities for clinical translation.

ASSOCIATED CONTENT

Supporting Information

The Supporting Information is available free of charge at https://pubs.acs.org/doi/10.1021/acscentsci.0c01097.

Materials and experimental details for the colloidal AuNST synthesis, APTES functionalization, *in situ* growth, capillary characterization, and cell release experiments, UV−visible, TEM and SEM characterization of nanoparticles optimized in solution and *in situ*, information on thermal analysis, additional SEM of cells on AuNSTs, and instrumentation setup information for the Raman/thermal and laser scanning confocal/thermal measurements (PDF)

Video S1: 10% laser power, no flow (MP4)

Video S2: 20% laser power, no flow (MP4)

Video S3: 30% laser power, no flow (MP4)

Video S4: 10% laser power, 50 μL/min flow (MP4)

Video S5: 20% laser power, 50 μL/min flow (MP4)

Video S6: 30% laser power, 50 μL/min flow (MP4)

Video S7: Negative control for a glass capillary functionalized with APTES and fibronectin, with no nanostars, at 30% laser power, no flow. (MP4)

Video S8: additional video of intact cell release (MP4)

https://dx.doi.org/10.1021/acscentsci.0c01097
ACS Cent. Sci. 2020, 6, 2105−2116

Video S9: additional video of intact cell release (MP4)

Video S10: additional video of intact cell release (MP4)

AUTHOR INFORMATION

Corresponding Authors

Leonardo Scarabelli − *Department of Chemistry and Biochemistry and California NanoSystems Institute, University of California, Los Angeles, Los Angeles, California 90095, United States;* orcid.org/0000-0002-6830-5893; Email: lscarabelli@icmab.es

Paul S. Weiss − *Department of Chemistry and Biochemistry, California NanoSystems Institute, and Materials Science and Engineering Department, University of California, Los Angeles, Los Angeles, California 90095, United States;* orcid.org/0000-0001-5527-6248; Email: psw@cnsi.ucla.edu

Steven J. Jonas − *California NanoSystems Institute, Department of Pediatrics, David Geffen School of Medicine, Children's Discovery and Innovation Institute, and Eli & Edythe Broad Center of Regenerative Medicine and Stem Cell Research, University of California, Los Angeles, Los Angeles, California 90095, United States;* orcid.org/0000-0002-8111-0249; Email: sjonas@ucla.edu

Authors

Gail A. Vinnacombe-Willson − *Department of Chemistry and Biochemistry and California NanoSystems Institute, University of California, Los Angeles, Los Angeles, California 90095, United States;* orcid.org/0000-0002-6897-6574

Naihao Chiang − *Department of Chemistry and Biochemistry and California NanoSystems Institute, University of California, Los Angeles, Los Angeles, California 90095, United States;* orcid.org/0000-0003-3782-6546

Yuan Hu − *California NanoSystems Institute and Mechanical and Aerospace Engineering Department, University of California, Los Angeles, Los Angeles, California 90095, United States*

Liv K. Heidenreich − *Department of Chemistry and Biochemistry and California NanoSystems Institute, University of California, Los Angeles, Los Angeles, California 90095, United States;* orcid.org/0000-0001-9724-1158

Xi Li − *Department of Chemistry and Biochemistry and California NanoSystems Institute, University of California, Los Angeles, Los Angeles, California 90095, United States; State Key Laboratory of Coordination Chemistry, School of Chemistry and Chemical Engineering, Nanjing University, Nanjing, Jiangsu 210023, P. R. China*

Yao Gong − *Department of Chemistry and Biochemistry and California NanoSystems Institute, University of California, Los Angeles, Los Angeles, California 90095, United States;* orcid.org/0000-0001-6434-9998

Derek T. Inouye − *Department of Chemistry and Biochemistry and California NanoSystems Institute, University of California, Los Angeles, Los Angeles, California 90095, United States*

Timothy S. Fisher − *California NanoSystems Institute and Mechanical and Aerospace Engineering Department, University of California, Los Angeles, Los Angeles, California 90095, United States;* orcid.org/0000-0002-8909-313X

Complete contact information is available at: https://pubs.acs.org/10.1021/acscentsci.0c01097

Author Contributions

The experiments were designed by G.A.V.-W., L.S., N.C., P.S.W., and S.J.J. G.A.V.-W and L.S. led the colloidal and *in situ* growth optimization, N.C. led and developed the setups for the concurrent Raman/thermal imaging and laser scanning confocal/thermal imaging characterizations. Data were collected by G.A.V.-W., L.S., N.C., L.K.H., X.L., Y.G., and D.T.I. Thermal analyses were performed by Y.H. and T.S.F. Figures were prepared by G.A.V.-W., L.S., N.C., and Y.H.. The manuscript was written by G.A.V.-W., L.S., N.C., P.S.W., and S.J.J., with assistance from all other authors. All authors have given approval to the final version of the manuscript.

Notes

The authors declare the following competing financial interest(s): G.A.V.-W, N.C., L.K.H., Y.G., L.S., P.S.W., and S.J.J. are inventors on US and international patent applications filed by the Regents of the University of California relating to the gold nanostar fluidic growth and application for cell release.

ACKNOWLEDGMENTS

The authors thank Prof. Vincent Tung (KAUST) and Prof. H. R. Tseng (UCLA) for helpful comments and discussion, as well as Prof. Bruce Dunn (UCLA) and the Broad Center of Regenerative Medicine & Stem Cell Research for providing access to the instrumentation for the Raman measurements. Facility support was provided by the UCLA Clinical and Translational Science Institute (CTSI) Core Voucher Program supported through Grant Number UL1TR001881. L.S. thanks the American-Italian Cancer Foundation for fellowship support. N.C. thanks the NIH NIBIB for the Pathway to Independence Award (K99EB028325). Y.G. thanks the UCLA Department of Chemistry & Biochemistry for funding through the SG Fellowship. X.L. thanks the UCLA Cross-Disciplinary Scholars in Science & Technology program. S.J.J. is supported by the NIH Common Fund through a NIH Director's Early Independence Award cofunded by the National Institute of Dental and Craniofacial Research and Office of the Director, NIH Grant DP5OD028181. S.J.J. also acknowledges Young Investigator Award funds from the Alex's Lemonade Stand Foundation for Childhood Cancer Research, the Hyundai Hope on Wheels Foundation for Pediatric Cancer Research, and the Tower Cancer Research Foundation. Confocal laser scanning microscopy was performed at the Advanced Light Microscopy/Spectroscopy Laboratory and the Leica Microsystems Center of Excellence at the California NanoSystems Institute (CNSI) at UCLA with funding support from NIH Shared Instrumentation Grant S10OD025017 and NSF Major Research Instrumentation Grant CHE-0722519. Special thanks to Dr. Laurent Bentolila, Dr. Michael Lake, and Dr. Matthew Schibler for their helpful discussions and instrumentation support critical to the completion of this work. The authors acknowledge the use of instruments at the Electron Imaging Center for NanoMachines supported by NIH (1S10RR23057) and CNSI at UCLA. We dedicate this paper to Prof. Laura Kiessling as part of a special collection, on the occasion of her birthday.

REFERENCES

(1) Hu, X.; Kwon, N.; Yan, K.; Sedgwick, A. C.; Chen, G.; He, X.; James, T. D.; Yoon, J. Bio-Conjugated Advanced Materials for Targeted Disease Theranostics. *Adv. Funct. Mater.* **2020**, *30*, 1907906.

(2) Langer, J.; Jimenez de Aberasturi, D.; Aizpurua, J.; Alvarez-Puebla, R. A.; Auguié, B.; Baumberg, J. J.; Bazan, G. C.; Bell, S. E. J.;

Boisen, A.; Brolo, A. G.; Choo, J.; Cialla-May, D.; Deckert, V.; Fabris, L.; Faulds, K.; García de Abajo, F. J.; Goodacre, R.; Graham, D.; Haes, A. J.; Haynes, C. L.; Huck, C.; Itoh, T.; Käll, M.; Kneipp, J.; Kotov, N. A.; Kuang, H.; Le Ru, E. C.; Lee, H. K.; Li, J.-F.; Ling, X. Y.; Maier, S. A.; Mayerhöfer, T.; Moskovits, M.; Murakoshi, K.; Nam, J.-M.; Nie, S.; Ozaki, Y.; Pastoriza-Santos, I.; Perez-Juste, J.; Popp, J.; Pucci, A.; Reich, S.; Ren, B.; Schatz, G. C.; Shegai, T.; Schlücker, S.; Tay, L.-L.; Thomas, K. G.; Tian, Z.-Q.; Van Duyne, R. P.; Vo-Dinh, T.; Wang, Y.; Willets, K. A.; Xu, C.; Xu, H.; Xu, Y.; Yamamoto, Y. S.; Zhao, B.; Liz-Marzán, L. M. Present and Future of Surface-Enhanced Raman Scattering. *ACS Nano* **2020**, *14*, 28−117.

(3) Guerrero-Martínez, A.; Barbosa, S.; Pastoriza-Santos, I.; Liz-Marzán, L. M. Nanostars Shine Bright for You. *Curr. Opin. Colloid Interface Sci.* **2011**, *16*, 118−127.

(4) Scarabelli, L. Recent Advances in the Rational Synthesis and Self-Assembly of Anisotropic Plasmonic Nanoparticles. *Pure Appl. Chem.* **2018**, *90*, 1393−1407.

(5) Niu, W.; Zhang, L.; Xu, G. Seed-Mediated Growth of Noble Metal Nanocrystals: Crystal Growth and Shape Control. *Nanoscale* **2013**, *5*, 3172−3181.

(6) Personick, M. L.; Langille, M. R.; Zhang, J.; Mirkin, C. A. Shape Control of Gold Nanoparticles by Silver Underpotential Deposition. *Nano Lett.* **2011**, *11*, 3394−3398.

(7) Xia, Y.; Xia, X.; Peng, H.-C. Shape-Controlled Synthesis of Colloidal Metal Nanocrystals: Thermodynamic versus Kinetic Products. *J. Am. Chem. Soc.* **2015**, *137*, 7947−7966.

(8) Xia, Y.; Gilroy, K. D.; Peng, H.-C.; Xia, X. Seed-Mediated Growth of Colloidal Metal Nanocrystals. *Angew. Chem., Int. Ed.* **2017**, *56*, 60−95.

(9) Grzelczak, M.; Pérez-Juste, J.; Mulvaney, P.; Liz-Marzán, L. M. Shape Control in Gold Nanoparticle Synthesis. *Chem. Soc. Rev.* **2008**, *37*, 1783−1791.

(10) Lohse, S. E.; Burrows, N. D.; Scarabelli, L.; Liz-Marzán, L. M.; Murphy, C. J. Anisotropic Noble Metal Nanocrystal Growth: The Role of Halides. *Chem. Mater.* **2014**, *26*, 34−43.

(11) Baffou, G.; Quidant, R. Thermo-Plasmonics: Using Metallic Nanostructures as Nano-Sources of Heat. *Laser Photonics Rev.* **2013**, *7*, 171−187.

(12) Ali, M. R. K.; Wu, Y.; El-Sayed, M. A. Gold-Nanoparticle-Assisted Plasmonic Photothermal Therapy Advances Toward Clinical Application. *J. Phys. Chem. C* **2019**, *123*, 15375−15393.

(13) Huang, X.; El-Sayed, I. H.; Qian, W.; El-Sayed, M. A. Cancer Cell Imaging and Photothermal Therapy in the Near-Infrared Region by Using Gold Nanorods. *J. Am. Chem. Soc.* **2006**, *128*, 2115−2120.

(14) Dam, D. H. M.; Lee, R. C.; Odom, T. W. Improved *in Vitro* Efficacy of Gold Nanoconstructs by Increased Loading of G-Quadruplex Aptamer. *Nano Lett.* **2014**, *14*, 2843−2848.

(15) Loo, C.; Lowery, A.; Halas, N.; West, J.; Drezek, R. Immunotargeted Nanoshells for Integrated Cancer Imaging and Therapy. *Nano Lett.* **2005**, *5*, 709−711.

(16) Hao, F.; Nehl, C. L.; Hafner, J. H.; Nordlander, P. Plasmon Resonances of a Gold Nanostar. *Nano Lett.* **2007**, *7*, 729−732.

(17) Barbosa, S.; Agrawal, A.; Rodríguez-Lorenzo, L.; Pastoriza-Santos, I.; Alvarez-Puebla, R. A.; Kornowski, A.; Weller, H.; Liz-Marzán, L. M. Tuning Size and Sensing Properties in Colloidal Gold Nanostars. *Langmuir* **2010**, *26*, 14943−14950.

(18) Rodríguez-Oliveros, R.; Sánchez-Gil, J. A. Gold Nanostars as Thermoplasmonic Nanoparticles for Optical Heating. *Opt. Express* **2012**, *20*, 621−626.

(19) Hua, Y.; Chandra, K.; Dam, D. H. M.; Wiederrecht, G. P.; Odom, T. W. Shape-Dependent Nonlinear Optical Properties of Anisotropic Gold Nanoparticles. *J. Phys. Chem. Lett.* **2015**, *6*, 4904−4908.

(20) Bhamidipati, M.; Cho, H.-Y.; Lee, K.-B.; Fabris, L. SERS-Based Quantification of Biomarker Expression at the Single Cell Level Enabled by Gold Nanostars and Truncated Aptamers. *Bioconjugate Chem.* **2018**, *29*, 2970−2981.

(21) Pallavicini, P.; Donà, A.; Taglietti, A.; Minzioni, P.; Patrini, M.; Dacarro, G.; Chirico, G.; Sironi, L.; Bloise, N.; Visai, L.; Scarabelli, L. Self-Assembled Monolayers of Gold Nanostars: A Convenient Tool for near-IR Photothermal Biofilm Eradication. *Chem. Commun.* **2014**, *50*, 1969−1971.

(22) Osinkina, L.; Lohmüller, T.; Jäckel, F.; Feldmann, J. Synthesis of Gold Nanostar Arrays as Reliable, Large-Scale, Homogeneous Substrates for Surface-Enhanced Raman Scattering Imaging and Spectroscopy. *J. Phys. Chem. C* **2013**, *117*, 22198−22202.

(23) Zhang, B.; Shi, Y.; Miyamoto, D.; Nakazawa, K.; Miyake, T. Nanostraw Membrane Stamping for Direct Delivery of Molecules into Adhesive Cells. *Sci. Rep.* **2019**, *9*, 6806−6814.

(24) Man, T.; Zhu, X.; Chow, Y. T.; Dawson, E. R.; Wen, X.; Patananan, A. N.; Liu, T. L.; Zhao, C.; Wu, C.; Hong, J. S.; Chung, P.-S.; Clemens, D. L.; Lee, B.-Y.; Weiss, P. S.; Teitell, M. A.; Chiou, P.-Y. Intracellular Photothermal Delivery for Suspension Cells Using Sharp Nanoscale Tips in Microwells. *ACS Nano* **2019**, *13*, 10835−10844.

(25) Giner-Casares, J. J.; Henriksen-Lacey, M.; García, I.; Liz-Marzán, L. M. Plasmonic Surfaces for Cell Growth and Retrieval Triggered by Near-Infrared Light. *Angew. Chem., Int. Ed.* **2016**, *55*, 974−978.

(26) Lv, S.-W.; Liu, Y.; Xie, M.; Wang, J.; Yan, X.-W.; Li, Z.; Dong, W.-G.; Huang, W.-H. Near-Infrared Light-Responsive Hydrogel for Specific Recognition and Photothermal Site- Release of Circulating Tumor Cells. *ACS Nano* **2016**, *10*, 6201−6210.

(27) Hirsch, L. R.; Stafford, R. J.; Bankson, J. A.; Sershen, S. R.; Rivera, B.; Price, R. E.; Hazle, J. D.; Halas, N. J.; West, J. L. Nanoshell-Mediated Near-Infrared Thermal Therapy of Tumors under Magnetic Resonance Guidance. *Proc. Natl. Acad. Sci. U. S. A.* **2003**, *100*, 13549−13554.

(28) Huang, X.; El-Sayed, I. H.; Qian, W.; El-Sayed, M. A. Cancer Cell Imaging and Photothermal Therapy in the Near-Infrared Region by Using Gold Nanorods. *J. Am. Chem. Soc.* **2006**, *128*, 2115−2120.

(29) Baffou, G.; Polleux, J.; Rigneault, H.; Monneret, S. Super-Heating and Micro-Bubble Generation around Plasmonic Nanoparticles Under cw Illumination. *J. Phys. Chem. C* **2014**, *118*, 4890−4898.

(30) Neumann, O.; Urban, A. S.; Day, J.; Lal, S.; Nordlander, P.; Halas, N. J. Solar Vapor Generation Enabled by Nanoparticles. *ACS Nano* **2013**, *7*, 42−49.

(31) Fang, Z.; Zhen, Y.-R.; Neumann, O.; Polman, A.; García de Abajo, F. J.; Nordlander, P.; Halas, N. J. Evolution of Light-Induced Vapor Generation at a Liquid-Immersed Metallic Nanoparticle. *Nano Lett.* **2013**, *13*, 1736−1742.

(32) Wang, D.; Bourgeois, M. R.; Guan, J.; Fumani, A. K.; Schatz, G. C.; Odom, T. W. Lasing from Finite Plasmonic Nanoparticle Lattices. *ACS Photonics* **2020**, *7*, 630−636.

(33) Gisbert Quilis, N.; Lequeux, M.; Venugopalan, P.; Khan, I.; Knoll, W.; Boujday, S.; Lamy de la Chapelle, M.; Dostalek, J. Tunable Laser Interference Lithography Preparation of Plasmonic Nanoparticle Arrays Tailored for SERS. *Nanoscale* **2018**, *10*, 10268−10276.

(34) Khabbaz Abkenar, S.; Tufani, A.; Ozaydin Ince, G.; Kurt, H.; Turak, A.; Ow-Yang, C. W. Transfer Printing Gold Nanoparticle Arrays by Tuning the Surface Hydrophilicity of Thermo-Responsive Poly *N*-Isopropylacrylamide (PNIPAAm). *Nanoscale* **2017**, *9*, 2969−2973.

(35) Velleman, L.; Sikdar, D.; Turek, V. A.; Kucernak, A. R.; Roser, S. J.; Kornyshev, A. A.; Edel, J. B. Tuneable 2D Self-Assembly of Plasmonic Nanoparticles at Liquid|Liquid Interfaces. *Nanoscale* **2016**, *8*, 19229−19241.

(36) Hamon, C.; Novikov, S.; Scarabelli, L.; Basabe-Desmonts, L.; Liz-Marzán, L. M. Hierarchical Self-Assembly of Gold Nanoparticles into Patterned Plasmonic Nanostructures. *ACS Nano* **2014**, *8*, 10694−10703.

(37) Ali Umar, A.; Oyama, M. Growth of High-Density Gold Nanoparticles on an Indium Tin Oxide Surface Prepared Using a "Touch" Seed-Mediated Growth Technique. *Cryst. Growth Des.* **2005**, *5*, 599−607.

(38) Kambayashi, M.; Zhang, J.; Oyama, M. Crystal Growth of Gold Nanoparticles on Indium Tin Oxides in the Absence and Presence of

https://dx.doi.org/10.1021/acscentsci.0c01097
ACS Cent. Sci. 2020, 6, 2105−2116

3-Mercaptopropyl-Trimethoxysilane. *Cryst. Growth Des.* **2005**, *5*, 81−84.
(39) Osinkina, L.; Lohmüller, T.; Jäckel, F.; Feldmann, J. Synthesis of Gold Nanostar Arrays as Reliable, Large-Scale, Homogeneous Substrates for Surface-Enhanced Raman Scattering Imaging and Spectroscopy. *J. Phys. Chem. C* **2013**, *117*, 22198−22202.
(40) Kumar, S.; Yang, H.; Zou, S. Seed-Mediated Growth of Uniform Gold Nanoparticle Arrays. *J. Phys. Chem. C* **2007**, *111*, 12933−12938.
(41) Fortuni, B.; Fujita, Y.; Ricci, M.; Inose, T.; Aubert, R.; Lu, G.; Hutchison, J. A.; Hofkens, J.; Latterini, L.; Uji-i, H. A Novel Method for *in Situ* Synthesis of SERS-Active Gold Nanostars on Polydimethylsiloxane Film. *Chem. Commun.* **2017**, *53*, 5121−5124.
(42) Cataldi, U.; Caputo, R.; Kurylyak, Y.; Klein, G.; Chekini, M.; Umeton, C.; Bürgi, T. Growing Gold Nanoparticles on a Flexible Substrate to Enable Simple Mechanical Control of Their Plasmonic Coupling. *J. Mater. Chem. C* **2014**, *2*, 7927−7933.
(43) Zhang, Q.; Xu, J.-J.; Liu, Y.; Chen, H.-Y. *In-Situ* Synthesis of Poly(Dimethylsiloxane)−Gold Nanoparticles Composite Films and Its Application in Microfluidic Systems. *Lab Chip* **2008**, *8*, 352−357.
(44) Jalali, M.; AbdelFatah, T.; Mahshid, S. S.; Labib, M.; Sudalaiyadum Perumal, A.; Mahshid, S. A Hierarchical 3D Nanostructured Microfluidic Device for Sensitive Detection of Pathogenic Bacteria. *Small* **2018**, *14*, 1801893.
(45) Li, Z.; Huang, X.; Lu, G. Recent Developments of Flexible and Transparent SERS Substrates. *J. Mater. Chem. C* **2020**, *8*, 3956−3969.
(46) Xiong, R.; Raemdonck, K.; Peynshaert, K.; Lentacker, I.; De Cock, I.; Demeester, J.; De Smedt, S. C.; Skirtach, A. G.; Braeckmans, K. Comparison of Gold Nanoparticle Mediated Photoporation: Vapor Nanobubbles Outperform Direct Heating for Delivering Macromolecules in Live Cells. *ACS Nano* **2014**, *8*, 6288−6296.
(47) Vanrompay, H.; Bladt, E.; Albrecht, W.; Béché, A.; Zakhozheva, M.; Sánchez-Iglesias, A.; Liz-Marzán, L. M.; Bals, S. 3D Characterization of Heat-Induced Morphological Changes of Au Nanostars by Fast *in Situ* Electron Tomography. *Nanoscale* **2018**, *10*, 22792−22801.
(48) Maestro, L. M.; Haro-González, P.; Sánchez-Iglesias, A.; Liz-Marzán, L. M.; García Solé, J.; Jaque, D. Quantum Dot Thermometry Evaluation of Geometry Dependent Heating Efficiency in Gold Nanoparticles. *Langmuir* **2014**, *30*, 1650−1658.
(49) Su, Q.; Ma, X.; Dong, J.; Jiang, C.; Qian, W. A Reproducible SERS Substrate Based on Electrostatically Assisted APTES-Functionalized Surface-Assembly of Gold Nanostars. *ACS Appl. Mater. Interfaces* **2011**, *3*, 1873−1879.
(50) Casu, A.; Cabrini, E.; Donà, A.; Falqui, A.; Diaz-Fernandez, Y.; Milanese, C.; Taglietti, A.; Pallavicini, P. Controlled Synthesis of Gold Nanostars by Using a Zwitterionic Surfactant. *Chem. - Eur. J.* **2012**, *18*, 9381−9390.
(51) Dhar, M.; Lam, J. N.; Walser, T.; Dubinett, S. M.; Rettig, M. B.; Di Carlo, D. Functional Profiling of Circulating Tumor Cells with an Integrated Vortex Capture and Single-Cell Protease Activity Assay. *Proc. Natl. Acad. Sci. U. S. A.* **2018**, *115*, 9986−9991.
(52) Che, J.; Yu, V.; Dhar, M.; Renier, C.; Matsumoto, M.; Heirich, K.; Garon, E. B.; Goldman, J.; Rao, J.; Sledge, G. W.; Pegram, M. D.; Sheth, S.; Jeffrey, S. S.; Kulkarni, R. P.; Sollier, E.; Di Carlo, D. Classification of Large Circulating Tumor Cells Isolated with Ultra-High Throughput Microfluidic Vortex Technology. *Oncotarget* **2016**, *7*, 12748−12760.
(53) Zhao, L.; Cheng, P.; Li, J.; Zhang, Y.; Gu, M.; Liu, J.; Zhang, J.; Zhu, J.-J. Analysis of Nonadherent Apoptotic Cells by a Quantum Dots Probe in a Microfluidic Device for Drug Screening. *Anal. Chem.* **2009**, *81*, 7075−7080.
(54) Komen, J.; Wolbers, F.; Franke, H. R.; Andersson, H.; Vermes, I.; van den Berg, A. Viability Analysis and Apoptosis Induction of Breast Cancer Cells in a Microfluidic Device: Effect of Cytostatic Drugs. *Biomed. Microdevices* **2008**, *10*, 727−737.
(55) Kyaw, H. H.; Al-Harthi, S. H.; Sellai, A.; Dutta, J. Self-Organization of Gold Nanoparticles on Silanated Surfaces. *Beilstein J. Nanotechnol.* **2015**, *6*, 2345−2353.
(56) Stoecklein, D.; Di Carlo, D. Nonlinear Microfluidics. *Anal. Chem.* **2019**, *91*, 296−314.
(57) Baffou, G. *Thermoplasmonics: Heating Metal Nanoparticles Using Light*; Cambridge University Press: Cambridge, U.K., 2017; pp 224−230.
(58) Jauffred, L.; Samadi, A.; Klingberg, H.; Bendix, P. M.; Oddershede, L. B. Plasmonic Heating of Nanostructures. *Chem. Rev.* **2019**, *119*, 8087−8130.
(59) Hou, L.; Yorulmaz, M.; Verhart, N. R.; Orrit, M. Explosive Formation and Dynamics of Vapor Nanobubbles around a Continuously Heated Gold Nanosphere. *New J. Phys.* **2015**, *17*, 013050.
(60) Kotaidis, V.; Dahmen, C.; von Plessen, G.; Springer, F.; Plech, A. Excitation of Nanoscale Vapor Bubbles at the Surface of Gold Nanoparticles in Water. *J. Chem. Phys.* **2006**, *124*, 184702.
(61) Jimenez de Aberasturi, D.; Serrano-Montes, A. B.; Langer, J.; Henriksen-Lacey, M.; Parak, W. J.; Liz-Marzán, L. M. Surface Enhanced Raman Scattering Encoded Gold Nanostars for Multiplexed Cell Discrimination. *Chem. Mater.* **2016**, *28*, 6779−6790.
(62) Meng, X.; Dyer, J.; Huo, Y.; Jiang, C. Greater SERS Activity of Ligand-Stabilized Gold Nanostars with Sharp Branches. *Langmuir* **2020**, *36*, 3558−3564.
(63) Bi, C.; Chen, J.; Chen, Y.; Song, Y.; Li, A.; Li, S.; Mao, Z.; Gao, C.; Wang, D.; Möhwald, H.; Xia, H. Realizing a Record Photothermal Conversion Efficiency of Spiky Gold Nanoparticles in the Second Near-Infrared Window by Structure-Based Rational Design. *Chem. Mater.* **2018**, *30*, 2709−2718.
(64) Espinosa, A.; Silva, A. K. A.; Sánchez-Iglesias, A.; Grzelczak, M.; Péchoux, C.; Desboeufs, K.; Liz-Marzán, L. M.; Wilhelm, C. Cancer Cell Internalization of Gold Nanostars Impacts Their Photothermal Efficiency *in Vitro* and *in Vivo*: Toward a Plasmonic Thermal Fingerprint in Tumoral Environment. *Adv. Healthcare Mater.* **2016**, *5*, 1040−1048.
(65) Muñoz-Pinedo, C.; Green, D. R.; van den Berg, A. Confocal Restricted-Height Imaging of Suspension Cells (CRISC) in a PDMS Microdevice during Apoptosis. *Lab Chip* **2005**, *5*, 628−633.
(66) Slaughter, L. S.; Cheung, K. M.; Kaappa, S.; Cao, H. H.; Yang, Q.; Young, T. D.; Serino, A. C.; Malola, S.; Olson, J. M.; Link, S.; Häkkinen, H.; Andrews, A. M.; Weiss, P. S. Patterning of Supported Gold Monolayers via Chemical Lift-off Lithography. *Beilstein J. Nanotechnol.* **2017**, *8*, 2648−2661.
(67) Malmsten, M. Ellipsometry Studies of Fibronectin Adsorption. *Colloids Surf., B* **1995**, *3*, 371−381.
(68) Wang, H.; Zhou, S.; Guo, L.; Wang, Y.; Feng, L. Intelligent Hybrid Hydrogels for Rapid *in Situ* Detection and Photothermal Therapy of Bacterial Infection. *ACS Appl. Mater. Interfaces* **2020**, *12*, 39685−39694.
(69) Moise, S.; Byrne, J. M.; El Haj, A. J.; Telling, N. D. The Potential of Magnetic Hyperthermia for Triggering the Differentiation of Cancer Cells. *Nanoscale* **2018**, *10*, 20519−20525.
(70) Zharov, V. P.; Mercer, K. E.; Galitovskaya, E. N.; Smeltzer, M. S. Photothermal Nanotherapeutics and Nanodiagnostics for Selective Killing of Bacteria Targeted with Gold Nanoparticles. *Biophys. J.* **2006**, *90*, 619−627.
(71) Vo-Dinh, T. Shining Gold Nanostars: From Cancer Diagnostics to Photothermal Treatment and Immunotherapy. *J. Immunol. Sci.* **2018**, *2*, 1−8.
(72) Crawford, B.; Shammas, R.; Fales, A.; Brown, D.; Hollenbeck, S.; Vo-Dinh, T.; Devi, G. Photothermal Ablation of Inflammatory Breast Cancer Tumor Emboli Using Plasmonic Gold Nanostars. *Int. J. Nanomed.* **2017**, *12*, 6259−6272.
(73) Pérez-Hernández, M.; del Pino, P.; Mitchell, S. G.; Moros, M.; Stepien, G.; Pelaz, B.; Parak, W. J.; Gálvez, E. M.; Pardo, J.; de la Fuente, J. M. Dissecting the Molecular Mechanism of Apoptosis during Photothermal Therapy Using Gold Nanoprisms. *ACS Nano* **2015**, *9*, 52−61.
(74) Díaz-Núñez, P.; González-Rubio, G.; Prada, A.; González Izquierdo, J.; Rivera, A.; Bañares, L.; Guerrero-Martínez, A.; Peña-

https://dx.doi.org/10.1021/acscentsci.0c01097
ACS Cent. Sci. 2020, 6, 2105−2116

Rodríguez, O. Using Femtosecond Laser Irradiation To Grow the Belly of Gold Nanorods. *J. Phys. Chem. C* **2018**, *122*, 19816−19822.
(75) Yan, J.; Zhu, D.; Xie, J.; Shao, Y.; Xiao, W. Light Tailoring of Internal Atomic Structure of Gold Nanorods. *Small* **2020**, *16*, 2001101.

https://dx.doi.org/10.1021/acscentsci.0c01097
ACS Cent. Sci. 2020, 6, 2105−2116